PERGAMON

International Journal of Heat and Mass Transfer 42 (1999) 581–597

International Journal of HEAT and MASS TRANSFER

Natural convection in a porous layer bounded by impervious domains: from numerical approaches to experimental realization

S. Chevalier[1,*], D. Bernard, N. Joly[2]

Laboratoire 'Energétique et Phénomènes de Transfert', L.E.P.T.-ENSAM (URA CNRS 873), Esplanade des Arts et Métiers, 33405 Talence Cedex, France

Received 27 May 1997; in final form 30 June 1998

Abstract

This work presents the results of a numerical and experimental study of free convection in a porous layer bounded by impervious domains subjected to a vertical temperature gradient. This configuration has been chosen as a reference for some geological structures. The main parameters of the experimental configuration are a slope of 15°, an aspect ratio of 10 for the porous layer and a thermal conductivity ratio (λ_p/λ_{np}) of 0.7. For that case, a good coherence is found concerning the flow patterns observed through the different methods. In all results, an anti-clockwise unicellular flow (with a layer rising from left to right) is observed at low filtration Rayleigh numbers Ra^*. At higher Ra^*, the three-dimensional (3D) flow which develops is composed of seven transversal (horizontal) rolls and five to seven longitudinal rolls. However, depending on the resolution method, the critical filtration Rayleigh numbers for the transition from 2D to 3D flows are significantly different. Moreover, the experimental temperature fields have some special features: a high amplitude of the unicellular flow and, for 3D flows, a low amplitude for the rolls in the central part of the layer and an even number of longitudinal rolls. Numerical resolutions taking into account the thermal heterogeneities of the experiment prove the significant influence of lateral thermal conditions on flow patterns and on the critical filtration Rayleigh number.

Nomenclature

e gravity unit vector
g gravity acceleration [m s^{-2}]
H thickness of the porous layer [m]
K permeability [m^2]
p pressure [Pa]
Ra^* filtration Rayleigh number
t time [s]
T temperature [K]
V filtration velocity [m s^{-1}].

Greek symbols
α dimensionless wave number
β fluid volumic expansion coefficient [1/K]
ΔT temperature difference [K]
θ dimensionless temperature perturbation
λ thermal conductivity [W m^{-1} K^{-1}]
Λ dimensionless thermal conductivity
μ dynamic viscosity [kg m^{-1} s^{-1}]
π dimensionless pressure perturbation
ρ mass density [kg m^{-3}]
(ρC) volumic thermal capacity [J m^{-3} K^{-1}]
σ inverse of time constant (s^{-1})
ω dimensionless velocity perturbation
ϕ sloping angle.

Superscripts and subscripts
c critical
f fluid
m marginal stability

* Corresponding author
[1] Present address: Laboratoire Environnement, Géomécanique et Ouvrages, Ecole Nationale Supèrieure de Géologie, B.P. 40, 54501 Vandœuvre-lès-Nancy, France.
[2] Present address: Institut d'Acoustique et de Mécanique, Université du Maine, Avenue Olivier Messiaen, 72085 Le Mans Cedex 9, France.

0017–9310/98 $19.00
PII: S0017–9310(98)00222–1

np impervious domain
p porous media
ref reference
y y direction
0 at the reference temperature
* equivalent property of the porous media.

1. Introduction

Natural convection is an omnipresent transport phenomenon in saturated porous geological structures. The local thermal conditions and the physical properties of media are directly of great importance on the characteristics of the heat and mass transfer in such real configurations. Moreover the nature of the fluid flow (2D, 3D, pattern and range) is drastically dependent on the complexity of geological sites, that means the geometry, heterogeneity and anisotropy of the domains.

Fluid motions induced by free convection have tangible effects in geothermal areas, on the diffusion of pollutants or on the mineral diagenesis processes. During the last thirty years, a substantial amount of fundamental research has been undertaken in order to identify the parameters that influence this mechanism. A complete summary of the subject was done by Nield and Bejan [1]. The first theoretical and experimental studies dealt with the reference configuration corresponding to a horizontal, infinite or of great lateral extensions, porous layer heated from below. The influence of the porous medium characteristics, fluid nature and of the thermal and hydrodynamic boundaries on flow patterns, on heat transfer (characterized by the Nusselt number) and on the range of temperature perturbations has been actively studied [1–6]. The slope of the layer is an additional parameter that influences the criterion of convective phenomenon [7–10].

The reference configuration described above is simple enough to allow its study both numerically and experimentally. However, this configuration is far from being representative of geological structures. The recent increase in computer capacity and the development of new numerical methods allows the study of more complex configurations. Therefore it is now possible to take into account the anisotropy and the presence of heat conducting domains bounding the porous layer [11–14]. Numerical modeling allows consideration of additional physical phenomena appearing in geological structures such as the transport of reactive solutions or the preferential fluid flows in the fault [15, 16]. However, the experimental validation of such models is most often impossible.

This paper presents the research conducted to define a reference configuration for geological structures allowing us to design and to conduct an experimental study. The selected reference configuration is a sloping porous layer bounded by impervious domains. Three different forms of the reference configuration are determined: (1) the infinite layer (2) the ideal finite layer (with adiabatic thermal conditions on lateral sides) and (3) the realistic finite layer (with lateral thermal losses). Three numerical approaches are considered to study the configurations: (1) direct 2D resolution (2) direct 3D resolution and (3) a stability analysis. All of these approaches are based on finite element theory. Firstly, the paper presents a brief summary of the mathematical theory and of the numerical methods used for the resolution of the natural convection phenomenon. Next, the numerical results for each method of resolution are presented depending on the studied configuration. In a third stage, the experiment, consisting of the realistic infinite layer is described and the original results are presented. Finally, the differences between numerical and experimental results are examined. The influence of the finite conducting boundaries and of the thermal lateral conditions are clarified.

2. The three different forms of the reference configuration

The reference configuration considered in this paper is a sloped porous layer bounded by impervious domains subjected to a vertical temperature gradient. It represents a model of the typical hydrogeological structures of confined aquifers. The following remarks underline the most frequently met characteristics for this kind of natural site. Generally the saturated porous media are bounded on the upper and lower sides by more or less impervious domains and, consequently, do not possess good heat-conducting boundaries. The thermal conductivity of these zones is often inferior to the equivalent thermal conductivity of the aquifer. The single phase saturating fluid is water. Most of these hydrogeological structures are inclined (anticlinal) and have great lateral extensions (the aquifer thickness is low in comparison with the other dimensions).

Some additional simplifications are used in the paper. All domains are assumed to be homogeneous and isotropic. Both totally impervious domains are assumed to have the same physical properties and particularly the same thermal conductivity. No hydraulic gradient is considered (no advection). Therefore, all obtained results are general and provide a global frame to estimate the behavior of real structures. These results are eventually extendible to more complex configurations taking into account the known effects of various slopes, geometry or anisotropic conditions. Furthermore, the simplifications mentioned above facilitate the experimental design.

Considering a layer's slope of fifteen degrees, three reference configurations have been defined with respect to the precedent considerations. The first one is the infinite layer. This configuration allows a 3D analytical study.

The second configuration concerns the ideal finite layer, which is presented in 3D in Fig. 1a. The finite dimensions correspond to a shape ratio of ten. The vertical sides of the configuration are assumed to be perfectly adiabatic. The upper and lower horizontal sides of the impervious domains are isothermal. The last configuration is the realistic finite layer which is defined in order to more adequately simulate the experimental conditions. The most significant difference between this configuration and the ideal finite layer concerns the thermal boundary conditions. In 2D modeling (Fig. 1b), the presence of insulating domains and external forced convection on lateral sides are considered. The thermal heterogeneities due to the impermeable medium around the fluid saturated porous layer (plastic frame) and to aluminium plates located in insulating domains (polyurethane foam) are taken into account (Section 6). The thermal conductivities for the different domains are presented in Table 1. In 3D modeling, in order to facilitate the computations, the thermal heterogeneities are taken into

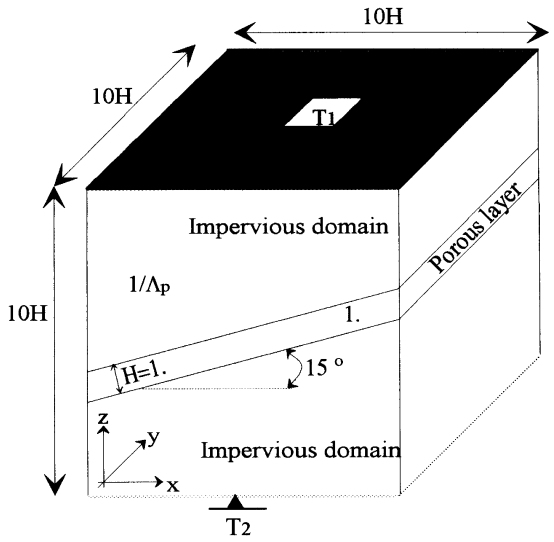

Fig. 1.a

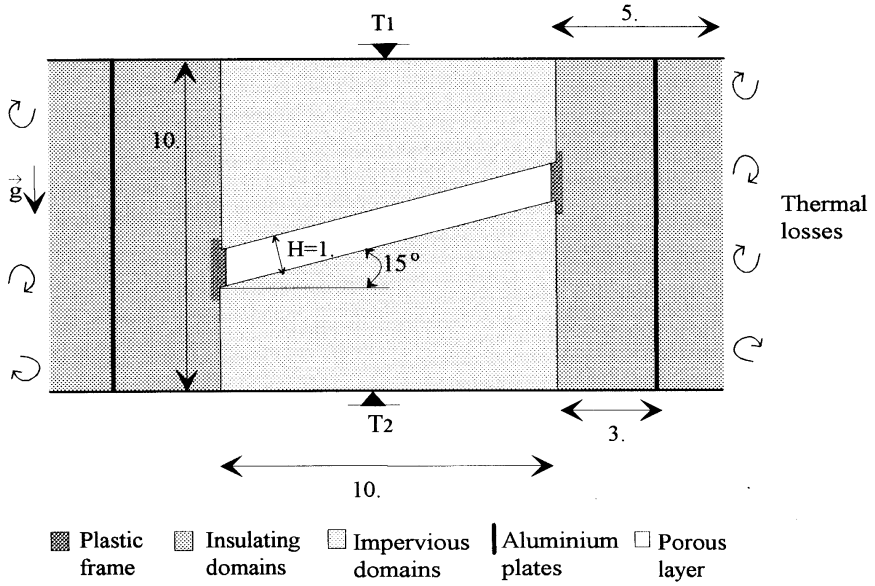

Fig. 1.b

Fig. 1. 3D dimensionless model of the ideal finite porous layer (1a) and 2D dimensionless model of the realistic finite porous layer (1b).

Table 1
Thermal conductivity of the different materials used in the experimental set-up

Materials	Thermal conductivity [W m^{-1} K^{-1}]
Saturated by water porous layer (glass bed) from [7]	$\lambda^* = 0.87$
Impervious domains (concrete blocks) measured at 30°C	1.25
Plastic frame	0.17
Aluminium plates	300
Polyurethane foam	0.021
Plastic springs	0.2

account imposing a mixed boundary condition with constant heat transfer coefficient at the porous layer's lateral sides. However, this simplification only allows to obtain a trend of the influence of imperfect adiabatic conditions on the phenomenon.

3. The mathematical models

3.1. Natural convection

The usual mathematical description of the natural convection phenomenon is composed of a set of four equations including the continuity equation, Darcy's law, the heat transfer equation and a simplified equation of state for the fluid [17]. The system of equations has been transformed into a dimensionless form, in order to simplify its resolution. In the following formulation, taking into account simplifications due to the considered reference configurations [18], the dimensionless filtration Rayleigh number Ra^* appears, equation (1.2). It quantifies the ratio between the driving forces for free convection $(\beta, g, \Delta T_{\mathrm{ref}})$ and stabilizing forces $(\mu_{\mathrm{f}}, \lambda_{\mathrm{ref}})$.

$$\nabla \cdot V = 0 \tag{1.1}$$

$$V = -(\nabla_p + Ra^* T\mathbf{e}) \tag{1.2}$$

$$\frac{\partial T}{\partial t} - \nabla \cdot (\underline{\underline{\Lambda}} \cdot \nabla T) + V \cdot \nabla T = 0$$

$$\text{with} \quad Ra^* = \frac{(\rho C)_{\mathrm{f}} k H \beta \rho_{\mathrm{f}} g}{\mu_{\mathrm{f}} \lambda_{\mathrm{ref}}} \Delta T_{\mathrm{ref}} \tag{1.3}$$

$\underline{\underline{\Lambda}}$ is the tensor corresponding to the ratio of the thermal conductivity of domains on the reference thermal conductivity and H is the reference length (porous layer thickness). The reference parameters used to obtain the system presented above are the physical properties of the fluid and the homogeneous and isotropic permeability of the porous medium. Different choices have been made for the reference thermal conductivity and the reference difference of temperature depending essentially on the thermal boundaries applied. It becomes obvious that the filtration Rayleigh number is not an intrinsic parameter of the porous configuration.

The formulation presented above implies some essential assumptions. The simple ones are that the porous matrix is rigid and that no geochemical reaction or compaction take place. The most important assumption is to consider that the flow value is low. This requirement is necessary to assume that Darcy's law and the local thermal equilibrium condition are valid, and that the thermal dispersion can be neglected [1, 17]. It is important to mention that these assumptions are generally justified in geological structures and specially where no forced flow is considered. The Boussinesq approximation is assumed to be valid. All the physical properties influencing the phenomenon are assumed to be constant, only the fluid density varies as a function of the temperature in the Darcy's law. The most restricting assumption is then to neglect the variations of fluid viscosity with temperature [19].

3.2. Stability analysis

Equations (1) can be solved directly in 2D or 3D using numerical methods. For the particular 3D configurations of which geometry is assumed to be reducible in 2D (the 3D geometry may be obtained by translation of the 2D configuration along the third direction), the 2D resolution seems to be appropriate. However, even in this case, the 2D solution obtained numerically may be unstable to 3D disturbances, meaning that this solution may never be observed in real 3D configuration. One way to proceed with the 2D convective study consists then in realizing a stability analysis as developed below.

To check the stability of a 2D steady state solution (T_0, P_0, V_0), an arbitrary infinitesimal perturbation (θ, π, ω) is superimposed to it. The disturbed state $(\theta + T_0, \pi + P_0, \omega + V_0)$, as the basic state, is a solution of equations (1). The resolution leads to equations (2) in which θ and π are periodic functions having the form presented in equations (3).

$$\nabla \cdot [\nabla \pi + Ra^* \theta \mathbf{e}] - \alpha^2 \pi = 0 \tag{2.1}$$

$$\sigma\theta - \nabla \cdot (\underline{\underline{\Lambda}} \cdot \nabla\theta) + [V_0 \cdot \nabla\theta - (\nabla\pi + Ra^*\theta\mathbf{e}) \cdot \nabla T_0] + \alpha^2 \Lambda_y \theta = 0 \tag{2.2}$$

The heat perturbation equation (2.2) has been linearized [13, 16]. To test the stability of the 2D basic state, we check for the existence of a solution (θ, π) of equations (2) which does not vanish for increasing time.

$$\pi = \pi_1(x, z) \cdot \mathrm{e}^{i\alpha y} \cdot \mathrm{e}^{\sigma t} \tag{3.1}$$

$$\theta = \theta_1(x, z) \cdot \mathrm{e}^{i\alpha y} \cdot \mathrm{e}^{\sigma t} \tag{3.2}$$

where α is the wave number in the third direction and σ the inverse of a time constant.

If all the perturbation solutions of equations (2) decay with time, the basic state is stable. The real solution is the 2D computed flow. If at least one perturbation grows with time, the basic state is unstable. The flow in the configuration is 3D. If the perturbations decay with time and only one is constant, a marginal stability state is defined, characterized by the critical parameters (Ra^*_c, α_c). The critical perturbation is the first which is able to develop in the configuration. Due to the linearization assumption, the computed perturbations have a sense only for infinitesimal amplitudes. However, the perturbation pattern and the critical associated wave number are representative of the 3D flow. The critical filtration Rayleigh number corresponds to the transition criterion from 2D convective flows to 3D. The assumption of linearization is nevertheless restrictive and may have some effects on the results. Therefore, the linear stability analysis does not act as a proper alternative to the 3D resolution.

4. Numerical resolution methods

4.1. Direct resolutions

An analytical formulation of the velocity and temperature gradient has been obtained for the unicellular flow (basic flow) in the configuration of the infinite layer. Its formulation is described by Bernard [20].

A numerical model simulating free convection, equations (1), has been developed around the general finite element program package [21]. Its first development is 2D and has been validated by Bernard [18]. It assumed that the configuration dimensions are finite and can be restricted to two dimensions. Domains are discretized in space using triangles. Temperature is approximated in all the domains by first order polynomials, whereas pressure is approximated by second order polynomials in porous domain (where mass transfer takes place). The time integration scheme is semi-implicit with constant time step. For the resolution, the reference parameters, equation (4), are the thermal conductivity of the porous medium and the ratio of the temperature difference between isothermal surfaces related to the dimensionless thickness separating them [22].

$$\lambda_{ref} = \lambda_p; \quad \Delta T_{ref} = \frac{T_2 - T_1}{10}$$

$$\Lambda_p = \frac{\lambda_p}{\lambda_{np}}; \quad Ra^*_{np} = \Lambda_p Ra^* \tag{4}$$

where Ra^*_{np} is the filtration Rayleigh number defined with the thermal conductivity of the impervious domain as reference parameter.

In the second stage, the 2D finite element model has been modified and developed in three dimensions. In this 3D version of the program, domains are discretized using tetrahedra. The resolution method is unchanged and the program has been validated by Chevalier [22].

4.2. Stability resolutions

Two methods have been developed in order to solve the perturbation system of equations.

The linear stability analysis of the analytical basic state has been performed by Joly [13] for the infinite layer configuration. The results are expressed in terms of critical filtration Rayleigh numbers and critical perturbations of the basic states. The mathematical approach which has been used, is based on Galerkin's method.

In the second method which has been applied to the 2D and 3D limited configurations, the problem is tackled numerically with the same finite element method than direct resolutions. Equations (2) can be finally reduced to an eigenvalue problem [23]. The unknown is the complex number representing the time expansion rate. The stability of a given basic state relatively to a given 3D perturbation (characterized by its wave number α) is determined by the sign of the real part of the expansion rate ($Re(\sigma_m)$), where σ_m is the eigenvalue having the largest real part. The basic state is stable for $Re(\sigma_m)$ negative, unstable if it is positive and the marginal stability state is reached for $Re(\sigma_m)$ equal to zero.

5. Numerical results

5.1. Two-dimensional convection

5.1.1. General results (all configurations)

Due to the slope of the layer and the thermal conductivity contrast between the domains, the purely conductive thermal gradient is not collinear to the gravity vector. Consequently, when Ra^* is different from zero, the conductive transfer does not solve equations (1), and consequently the convective flow must be present. The flow pattern which first appears (for small thermal perturbations and low Ra^*) corresponds to a single 2D cell. The fluid moves along the layer slope and the flow direction is determined by the ratio of the thermal conductivities [18]. For a layer rising from left to right, if the thermal conductivity of the porous medium is higher than impervious domains one, flow starts with a clockwise rotation (Fig. 2b), otherwise flow takes place with a counter-clockwise rotation (Fig. 2a).

5.1.2. The ideal finite configuration

Depending on the values of Ra^* and Λ_p, three flows have been determined: the counter-clockwise and clockwise unicellular flows and a polycellular (transversal

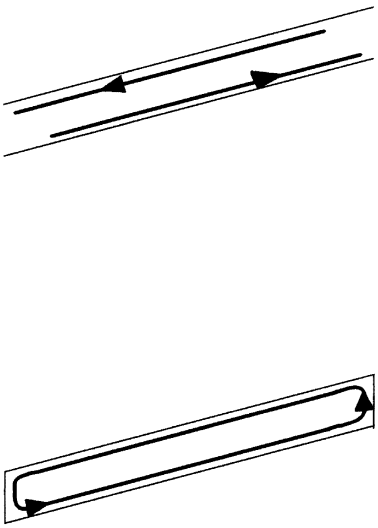

Fig. 2.a

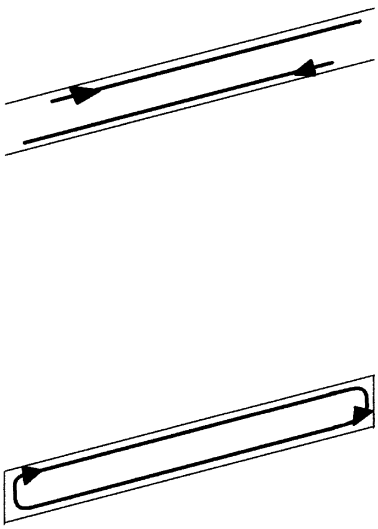

Fig 2.b

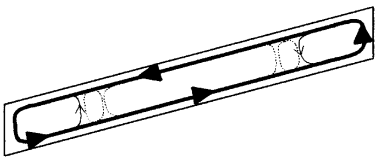

Fig.2.c

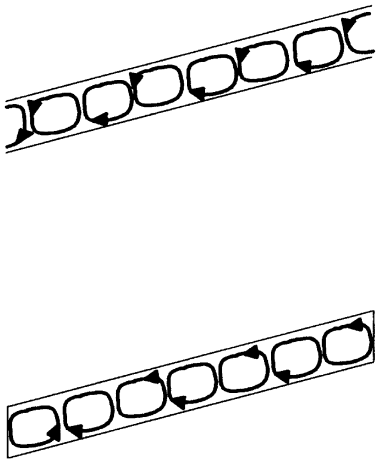

Fig.2.d

Fig. 2. Examples of different flow patterns depending on the configurations and Ra^*. (a) clockwise unicellular flow obtained for 2D and 3D infinite (no cell closure) and finite configurations at low Ra^* and $\Lambda_p < 1$; (b) counter-clockwise unicellular flow obtained for 2D and 3D infinite (no cell closure) and finite configurations at low Ra^* and $\Lambda_p > 1$; (c) intermediate state (transition from unicellular to polycellular flow) obtained for the 2D finite configurations; (d) 2D polycellular flow obtained for the infinite and finite (integer number of rolls) configurations at high Ra^*.

cells) pattern (Fig. 2d). The computed flow patterns are presented in Fig. 3 as a function of Ra^*_{np} and Λ_p values. It is not obvious to define clearly a single value of Ra^* at which the flow becomes polycellular. The flow changes from the unicellular state (Fig. 2a) to a polycellular one (Fig. 2d) through a 2D transition pattern (Fig. 2c). This intermediate state corresponds to the appearance of a cell at each lateral side of the porous layer (Fig. 2c). For the particular value of $\Lambda_p = 0.7$, the flow changes from the 2D unicellular pattern to a polycellular (3D) one through a transition state corresponding to Ra^*_{np} values ranging from 6 to 12.

5.1.3. The realistic finite configuration

The thermal heterogeneities of the experimental configuration (Fig. 1b) have the effects stated below, on 2D numerical results. The existence of the polyurethane foam (imperfectly adiabatic conditions) has no influence on

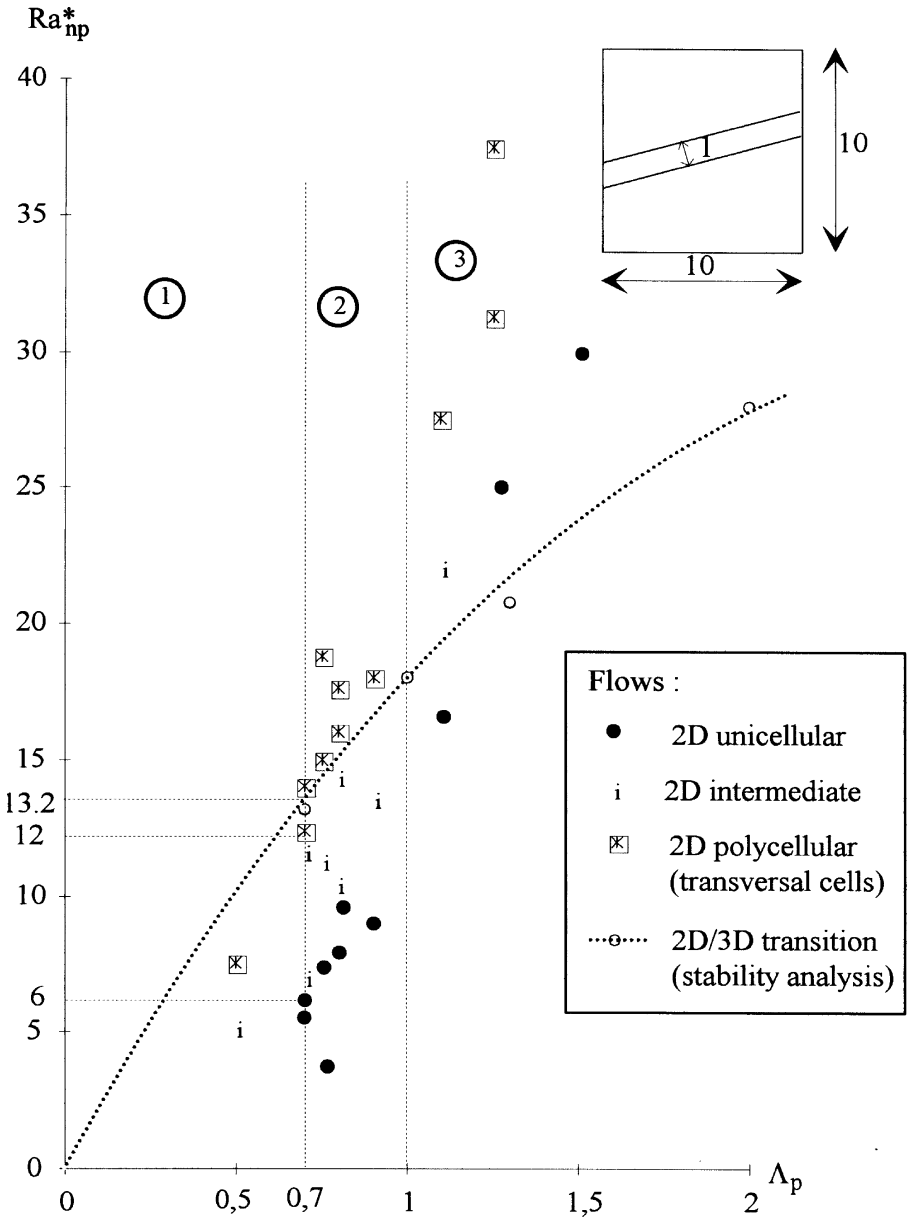

Fig. 3. Different 2D flow patterns and the 2D/3D stability curve obtained for the ideal finite layer as a function of Ra^* and Λ_p. Above the curve, all flows are three-dimensional. If $\Lambda_p < 0.7$ (zone 1), a flow composed of transversal rolls appears for some Ra^* values inferior to the 2D/3D transition filtration Rayleigh number. If $\Lambda_p > 1$, no transversal roll flow exist.

flow patterns and on the range of the convective motions. However, the Ra^* value of the unicellular flow disappearance is inferior to the ideal one. The presence of the plastic frame on the layer's borders has a little effect on temperature fields. A maximal variation of 2% is reached between the temperature fields corresponding to simulations with and without the frame. External air convection has no influence on the results, due to the low thermal conductivity of the insulating domains. This study of the realistic finite configuration establishes only a weak influence of the imperfect adiabatic conditions on the 2D numerical results.

5.2. Three-dimensional convection

5.2.1. The ideal finite configuration

The direct 3D computations allow us to determine three significant characteristics of the flows in the ideal finite layer at $\Lambda_p = 0.7$:

- No purely 2D polycellular flow exists. The unicellular flow changes directly into a 3D state. A roll appears at each side of the porous layer around the same Ra^* value in the two directions. The first longitudinal rolls which appear in the medium are then located along the two lateral sides of the medium.
- The 3D computations lead to higher values of the thermal perturbations (differences between conductive and convective temperature fields) than the 2D. The difference is negligible for low filtration Rayleigh number, it grows significantly with Ra^*, as the 2D solutions become unstable. At $Ra^* = 19.2$, the maximal 3D temperature perturbation is 3.6 versus 2.5°C in 2D.
- The projections of the velocity field onto the layer middle longitudinal and transversal sections are presented in Fig. 4 for $Ra^* = 19.2$. The 3D steady state flow pattern (elementary components) appears clearly. It consists of seven longitudinal and seven transversal rolls.

5.2.2. The realistic finite configuration

In order to understand the differences between experimental (Section 6) and 3D numerical temperature fields, an imperfect adiabatic condition has been used for some 3D computations. A mixed boundary condition with constant heat transfer coefficient has been imposed at the porous layer's lateral sides. The coefficient represents about one hundredth of the free convection transfer coefficient existing on a wall surface in a confined room. Figure 5 allows us to qualitatively compare the temperature perturbation fields in the middle plane of the porous layer for the two configurations with perfect (Fig. 5a) and imperfect (Fig. 5b) adiabatic conditions. The particular condition of thermal loss favors the development of longitudinal rolls (i.e. favors the 2D/3D transition). An additional longitudinal roll appears and the value of the longitudinal thermal perturbation almost doubles. These 3D numerical results suggest that the existence of the supplementary roll is due to the imperfect adiabaticity of the sides and that such conditions reduce the filtration Rayleigh number value of the 3D flow onset. The symmetrical thermal losses indeed lead necessarily to an even number of longitudinal rolls due to the downward flow at the ends of the horizontal sides.

5.3. Stability analysis

5.3.1. The infinite layer

Some qualitative differences, presented below, are noticeable between the stability conditions of the infinite and ideal finite configuration flows. The porous layer extension has a direct influence on the pattern of the perturbations. It controls the finite number of rolls (Fig. 2d) which can develop in the medium (i.e. the wave numbers of the disturbances). Moreover it must be sufficiently large to neglect the effects of the flow loops on the lateral borders of the porous domain (Fig. 2a and b). The influence of the cell loop on the velocity and temperature fields has been analyzed through comparison of results from infinite (analytical) and ideal finite (numerical) configurations [23]. The variations in the velocity range are low. However the changes in thermal fields are significant. The temperature perturbations due to the convective loop (differences between temperature fields of finite and infinite configurations) are, near the border of the layer, of the same magnitude as the perturbations due to the global convective motion (differences between conductive and convective temperature fields). The differences are not only located on the borders of the porous layer but in all the domains due to the diffusion phenomenon. General quantitative results concerning the transition from unicellular to polycellular flow have been obtained for an infinite layer inclined by 15°. If the value of Λ_p is inferior to 0.4, the perturbation motions first appear as longitudinal rolls. If the value of Λ_p is superior to 0.4, the perturbation motions appear in the form of horizontal rolls [13].

5.3.2. The ideal finite configuration

From the stability curve presented in Fig. 3, it can be deduced that for Λ_p values superior to 1 (common configuration of geological structures) no 2D polycellular flow exists. The unicellular flow changes directly into a 3D state; the longitudinal rolls for Ra^* values that are less or equal than Ra^* values corresponding to the transversal rolls appearance. The possibility of an established polycellular flow exists only for low Λ_p values (<0.7). For the experimental conductivity ratio ($\Lambda_p = 0.7$), the critical filtration Rayleigh number Ra_c^* for the 2D/3D transition is about 18.9 ($Ra_{np}^* = 13.2$). The basic flow for this Ra^* value belongs to the intermediate state. This result leads to the conclusion that the transversal rolls at the lateral

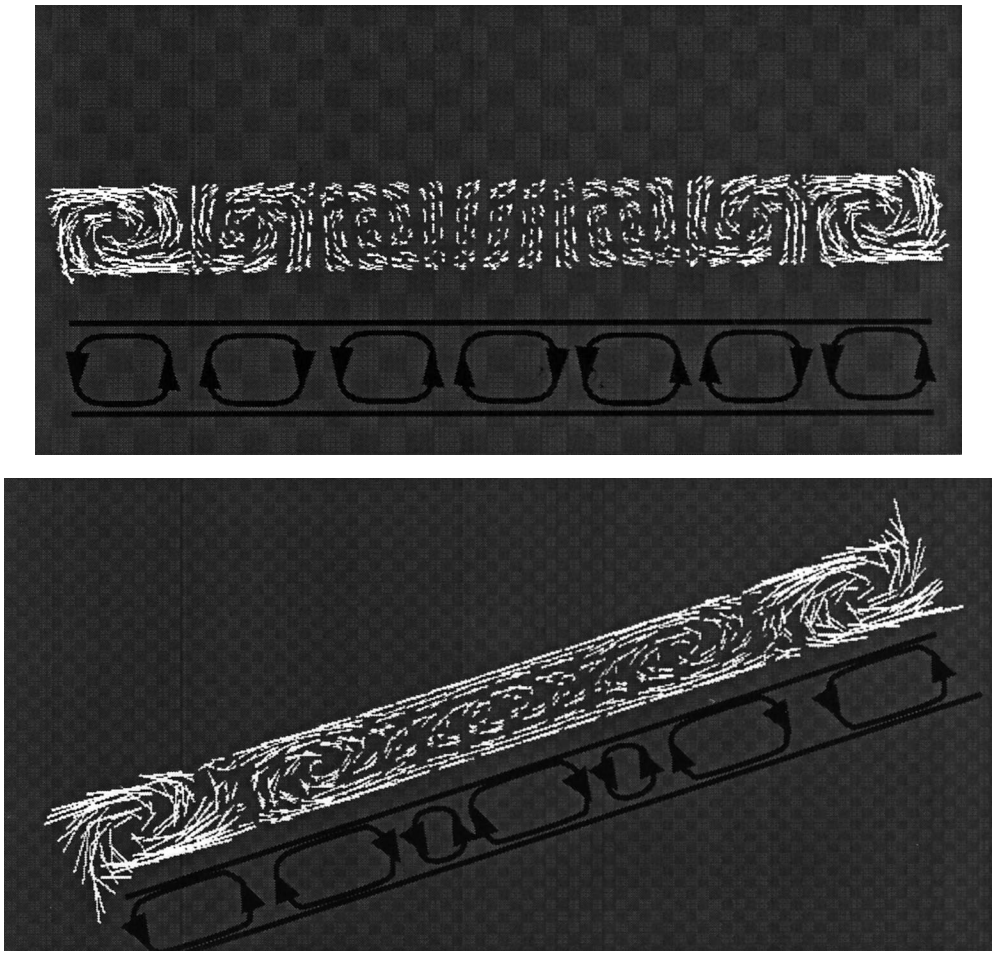

Fig. 4. Transversal (4a) and longitudinal (4b) sections of the velocity field in the middle of the 3D ideal finite layer at $\Lambda_p = 0.7$ and $Ra^* = 19.2$.

sides of the porous layer appear almost at the same time as the flow becomes three dimensional. Consequently, it is difficult to conclude the order of appearance of longitudinal and transversal rolls.

The temperature field of the critical perturbation in the middle plane of the porous layer ($\Lambda_p = 0.7$, $Ra_c^* = 18.9$) is presented in Fig. 6. The infinitesimal perturbations which are able to develop are composed of five longitudinal rolls.

5.3.3. The realistic finite configuration

Due to the influence of all experimental heterogeneities, the critical filtration Rayleigh number for the 2D/3D transition is higher for the realistic finite configuration ($Ra_c^* = 19.2$) than for the ideal one: the polycellular 2D flow is more stable. The occurrence interval for the polycellular flow increases in terms of the filtration Rayleigh number but the critical perturbation pattern is unchanged. These computations demonstrate that the thermal heterogeneities of the experimental configuration favor the appearance of transversal rolls.

6. The experiment

6.1. The experimental set-up

6.1.1. Materials

All thermal characteristics of the materials are summarized in Table 1, and the global experimental apparatus is presented in Fig. 7. All materials are assumed to be homogeneous and isotropic.

A square bed of sieved glass beads constitutes the porous layer. The filtered spheres are size-homogeneous with an average diameter of 2 mm. The bed has been vibrated during its creation and the uniform ordering of spheres has been visually verified. The resulting porosity was measured and found to be of the order of 33% and

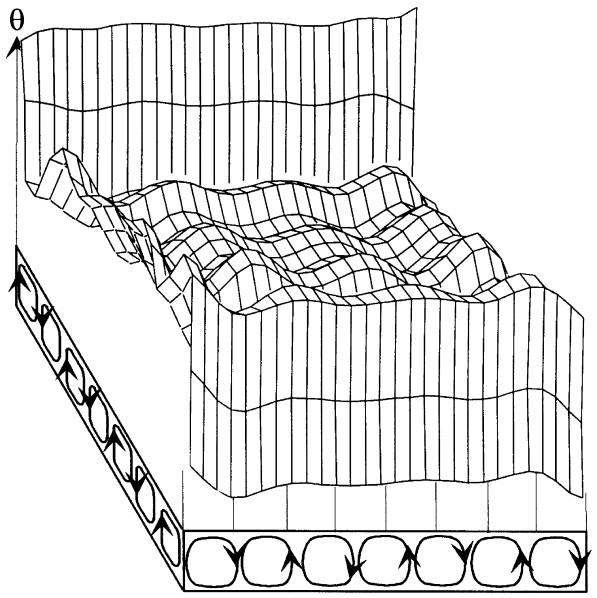

Fig. 5.a

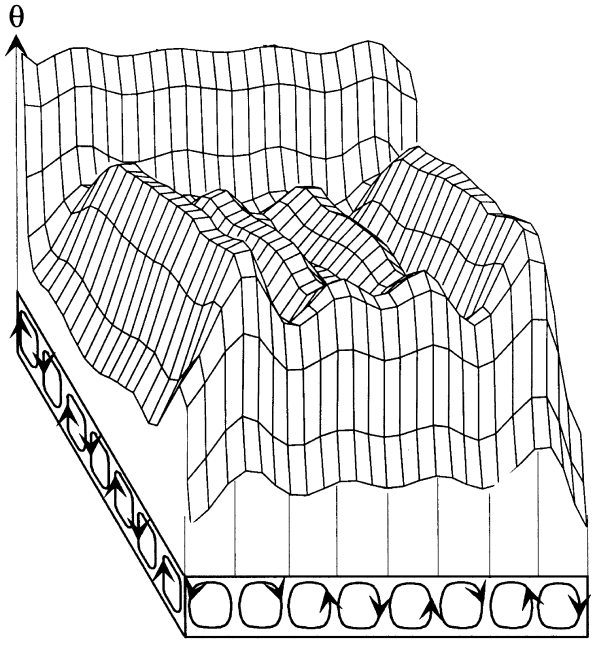

Fig. 5. b

Fig. 5. Temperature perturbation fields (convective–conductive thermal fields) in the middle plane of the configurations at $\Lambda_p = 0.7$ and $Ra^* = 19.2$; (a) ideal finite layer configuration; (b) realistic finite layer configuration. The longitudinal rolls located on the borders of the layer have a significantly higher amplitude than central ones.

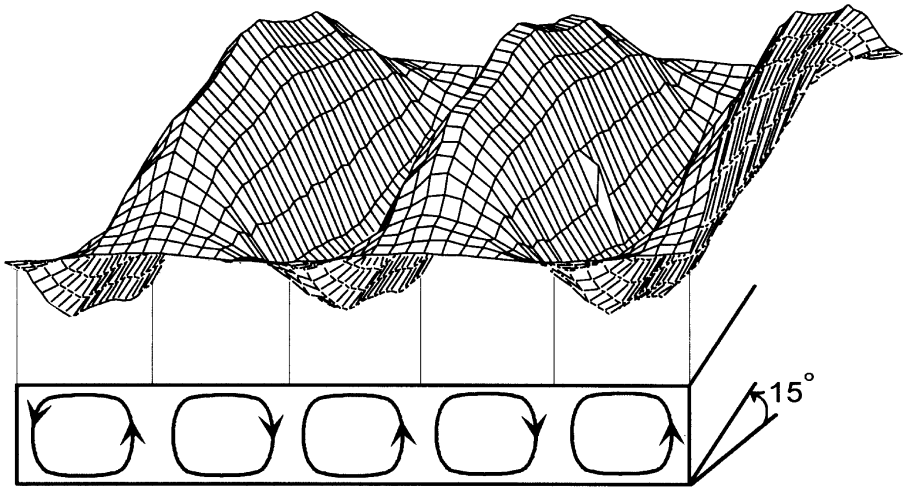

Fig. 6. Temperature field of the critical perturbation in the middle plane of the porous layer for the ideal finite layer ($Ra^*_{np} = 18.9$ and $\Lambda_p = 0.7$).

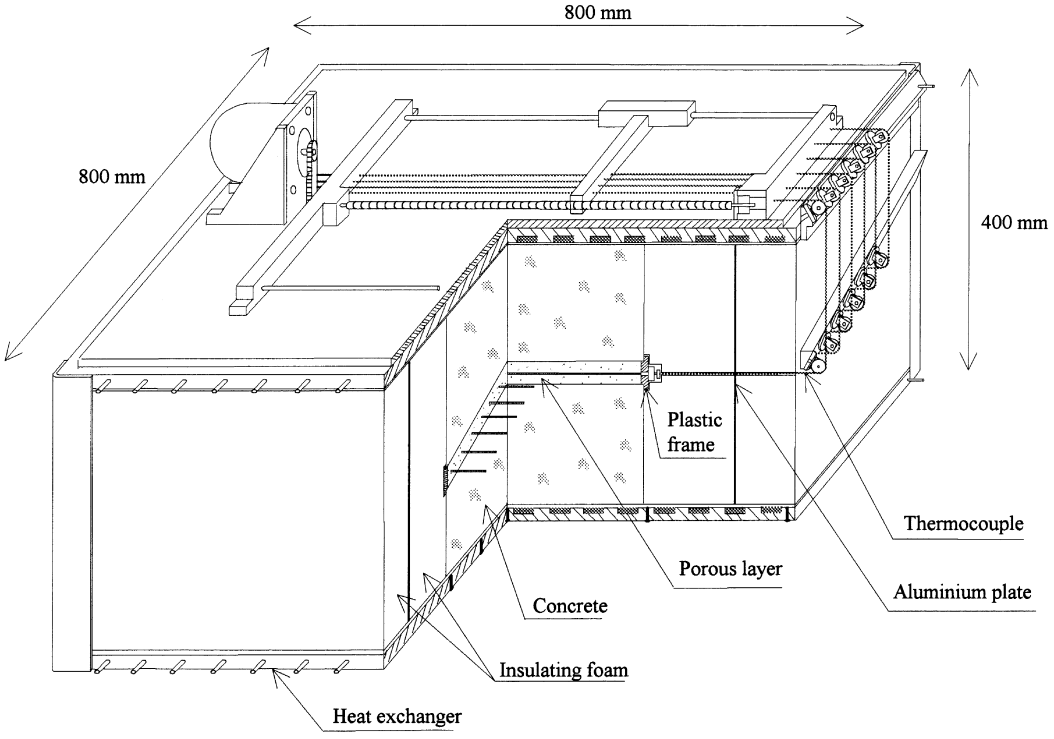

Fig. 7. Experimental set-up.

the calculated permeability (Kozeny–Carman equation) is 2.5×10^{-9} m^2. The side length of the bed is 400 mm, its thickness is 40 mm (shape ratio of 10); moreover, the layer is inclined at an angle of 15°. Air in the layer has been evacuated by a vacuum pump and the medium has been saturated by distilled and desaerated water. A water tank maintains the medium in a weak overpressure state and avoids any entry of air. A thin plastic frame (PVDF) maintains the filling around the porous medium. Its dimensions (60 mm wide and 10 mm thick) have been minimized to limit the disturbances of the thermal boundary condition perpendicularly to the layer.

Two concrete blocks bound the glass bed on its upper and lower sides to realize the thermal conducting boundaries. The interfaces between blocks and layer have been waterproofed. These three domains represent the cubic core of the experimental cell. The concrete has been vibrated during block formation to obtain homogeneous domains. The uniform granular distribution inside the blocks was visually verified after destroying a test block.

Two water flow based heat-exchangers maintain the uniform temperature conditions at the horizontal limits of the impervious blocks.

The adiabatic boundary condition on vertical sides is approximately realized using polyurethane foam (200 mm thick). Thin vertical aluminium plates divide the foam in two parts and connect both exchangers drastically limiting heat losses from the center to the exterior.

6.1.2. Temperature measurement system

The fluid temperature is measured in the middle plane of the porous layer using 14 thermocouples (E type) which are placed in plastic (PVC) springs in order to make them mobile within the porous medium. Seals prevent water leakage at the outlets of the thermocouples from the porous layer. The springs have an outside diameter of 3 mm and are made out of 1 mm thread. They have been set and glued on the plastic frame before the setting of the glass spheres. Rigid metal rods have been placed in the springs to avoid displacements when vibrating the bed. The space between two consecutive spirals of stretched springs is about 1 mm. With such characteristics, porosity and thermal perturbations due to the use of springs are limited.

Fourteen thermocouple measurement positions are available in the inclined direction and a quasi-infinite number of positions is possible in the horizontal direction (direction of the 3D flow occurrence). The thermocouple disposition is regular in the middle plane of the porous layer between the upper and lower lateral sides of the medium with an interval of 30 mm. The foam blocks and aluminium plates on two sides are drilled to allow the thermocouple movements.

A system composed of a step-by-step motor, an endless screw and four series of pulleys drag the thermocouples through the medium. The reading, recording and processing of experimental data are done using a Hewlett Packard data-acquisition (scanner) connected to a personal computer. Displacements and data-acquisitions are managed by a Turbo-Pascal program. The scanner resolution is equal to one microvolt and the sensitivity of the thermocouples to 60 μV $^{\circ}$C^{-1} at 40°C.

A thermocouple has been located in the middle of each concrete block and at their interfaces with the exchangers. This allows us to control the exchangers temperature and the evolution of the thermal characteristics of each block. The temperature measurement system is composed of 18 thermocouples, a thermometer, three temperature regulating baths (one for each exchanger and one for the reference temperature) and a scanner. The accuracy of the global system was determined to be 0.2°C in absolute temperature and 0.1°C between the measurements of two thermocouples.

The experimental equipment is kept in an air-conditioned room (control of temperature and air humidity).

6.1.3. Methodology

The temperature measurements are taken along horizontal lines with regular intervals of 10 mm. After several tests, the following optimal (minimal thermal perturbation and minimal total duration) measurement cycle has been chosen:

- displacement to the new measurement point (17 s),
- pause for local perturbation diffusion (43 s),
- measurement.

Acquisition of a complete temperature field needs 37 min.

To obtain the variations of the filtration Rayleigh number Ra^*, the upper side temperature is decreased and the lower side temperature is increased around the average temperature T_0 (40°C for these tests) using increments of 5°C. After a temperature change, 4–6 days are needed to stabilize the temperature field depending on a value of Ra^* (the temperature field is stabilized if the measured variation is lower than 0.2°C in 24 h).

For illustrative purposes, the grids of measures are treated as grids of numerical results. Each experimental measure location is considered as a computation node.

6.2. Results

The thermal fields obtained experimentally for different values of Ra^* (in the middle plane of the porous layer) are presented in Fig. 8. The elementary components of the corresponding flows, deduced from the field shapes are drawn on the same figure. For $Ra^* = 5.5$, the measured temperature field corresponds to the basic unicellular flow along the slope direction. The cell closure has no significant effect on the sides of the temperature plane. For $Ra^* = 8.3$, two longitudinal rolls appear along the sloped borders of the layer. The influence of the unicellular flow on the temperature field is now discernible. For $Ra^* = 11$, two additional transversal rolls modify the unicellular flow. For $Ra^* = 19.3$, whole flow is 3D. Whatever the filtration Rayleigh number values are, the influence on temperature fields of the central rolls is limited. Moreover, it is difficult to distinguish the presence of the unicellular flow for low Ra^* and the appearance of the first transversal and longitudinal rolls due to the measurements imprecision (0.2°C).

The filtration Rayleigh number values corresponding to the different flow patterns experimentally determined are shown in Fig. 9. At Ra^* value less than 8, the flow is unicellular. At Ra^* value greater than 11, the flow is

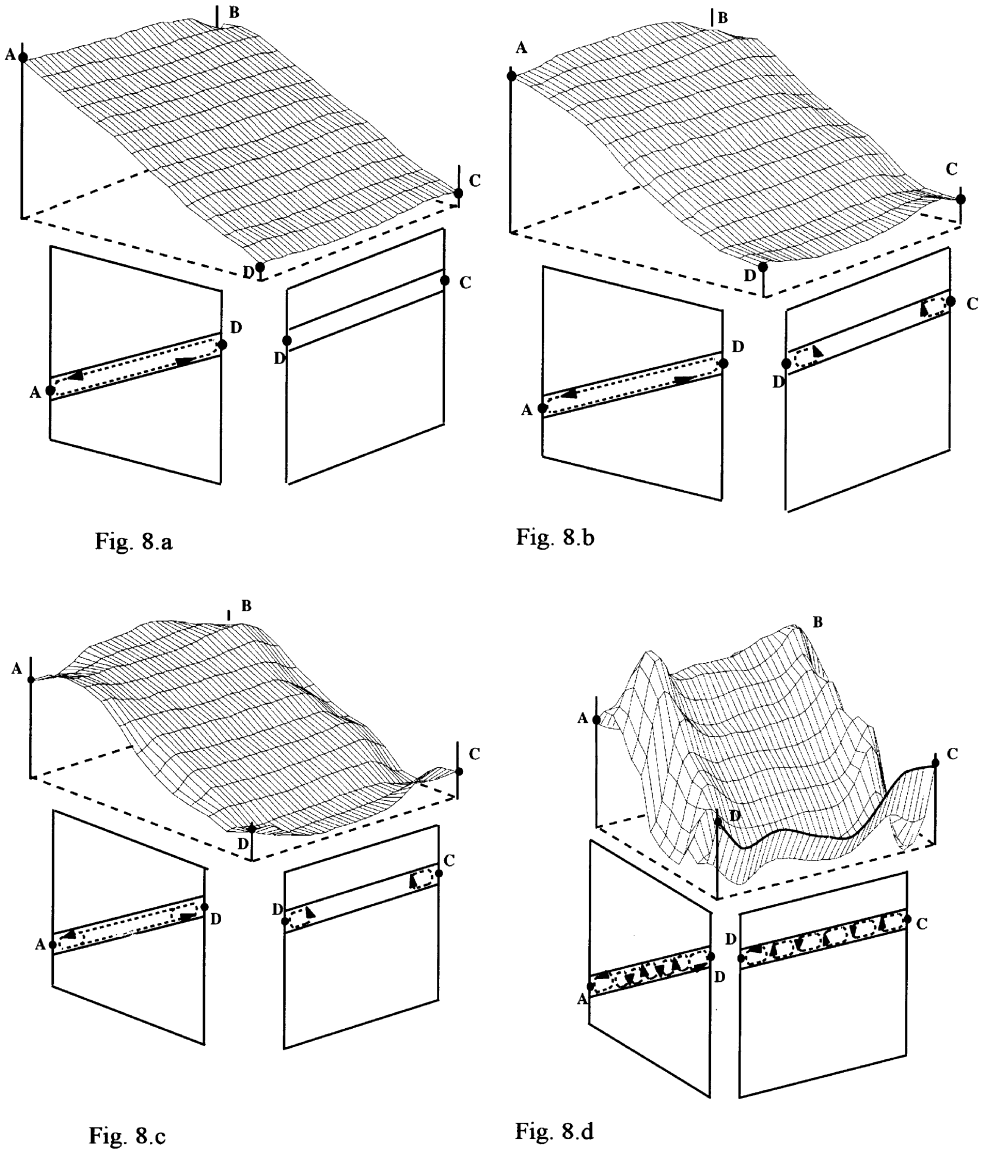

Fig. 8. Experimental temperature fields in the middle plane of the porous layer and the elementary components of associated flows for $Ra^* = 5.5$ (a); $Ra^* = 8.3$ (b); $Ra^* = 11$ (c) and $Ra^* = 19.3$ (d).

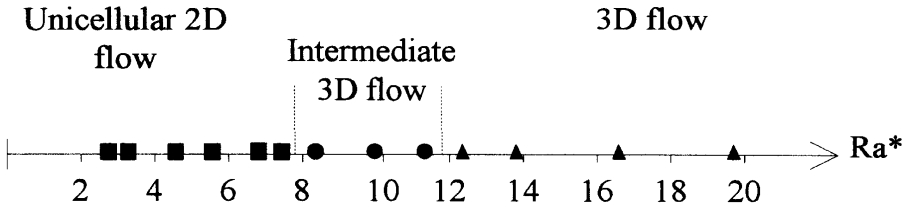

Fig. 9. Experimental flow patterns depending on Ra^* at $\Lambda_p = 0.7$. Each sign corresponds to an experimental result.

strictly 3D. In the interval between 8 and 11, the flow consists of the unicellular pattern plus longitudinal and transversal rolls along the borders of the layer.

The thermal perturbation amplitudes of the experimental fields are obtained by subtracting from the temperature fields temperature average planes approximately corresponding to the thermal conductive fields. The thermal perturbation visualizations allow us to distinguish more clearly the different flow patterns and so to infer the critical filtration Rayleigh number. The most significant perturbations are located on the borders of the porous layer. For low filtration Rayleigh numbers, the maximal temperature perturbations due to the unicellular flow are about 10 times the variations computed by 2D and 3D numerical resolutions ($Ra^* = 10, \Delta T \sim \pm 2.2^\circ C$). For Ra^* values corresponding to a 3D flow, the higher perturbations are doubled comparatively to 3D numerical ones ($Ra^* = 19.3, \Delta T \sim \pm 7^\circ C$). In the central part of the field, the perturbation amplitudes reach the measure precision.

For $Ra^* = 19.3$ (Figs 8d and 10), three-dimensional flow patterns are more clearly put into evidence using temperature perturbation. The flow can be broken up into following elementary motions: a transversal flow including the basic unicellular flow and seven secondary rolls, and, two important longitudinal rolls along the sloped borders of the layer and four superimposed central rolls.

7. Discussion

7.1. 2D/3D stability domains

In Fig. 11, the occurrence domains of the different flow patterns are presented, for the finite configurations, in terms of Ra^* values and as a function of the different resolution methods. The critical filtration Rayleigh number Ra_c^* for the onset of the 3D flow is superior in the stability study ($Ra_c^* = 19$) to the value obtained by the 3D direct computations ($Ra_c^* = 18$). The difference may be imputable to the linearity assumption. The non-linear term omission leads to an overvaluation of the 2D/3D transition critical Rayleigh number. The experimental value of Ra_c^* is inferior to the 3D computed value. The 2D results concerning the realistic finite layer prove that the transition from unicellular to polycellular flow appears for a lower Ra^* value than the ideal one due to the thermal heterogeneities. Moreover, the 3D results concerning the realistic finite layer prove that the tran-

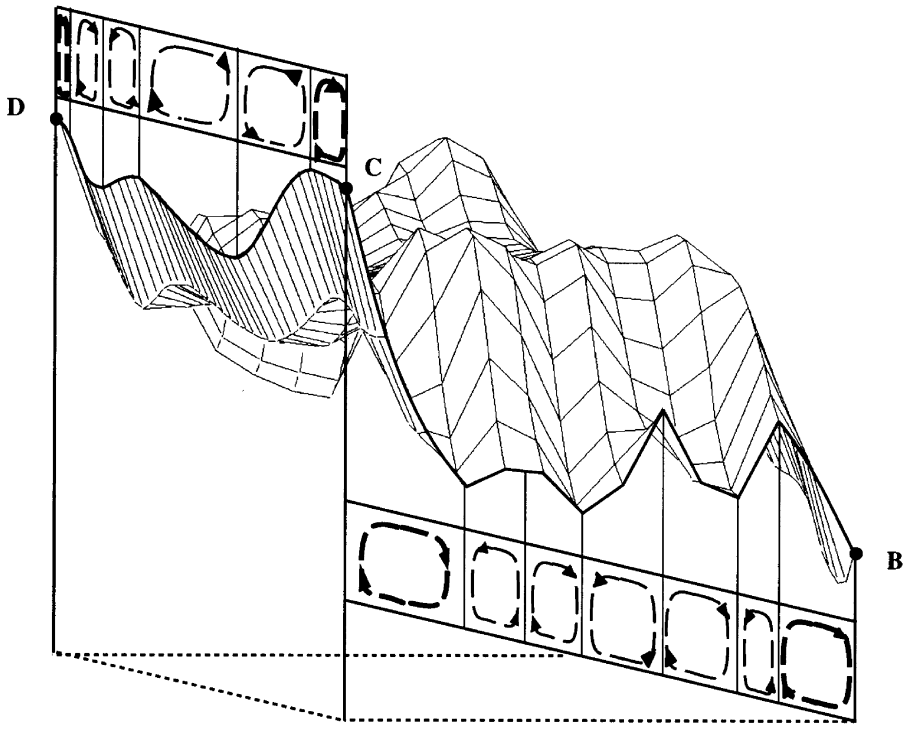

Fig. 10. Elementary component of the experimental 3D flow and temperature perturbation field for $Ra^* = 19.3$.

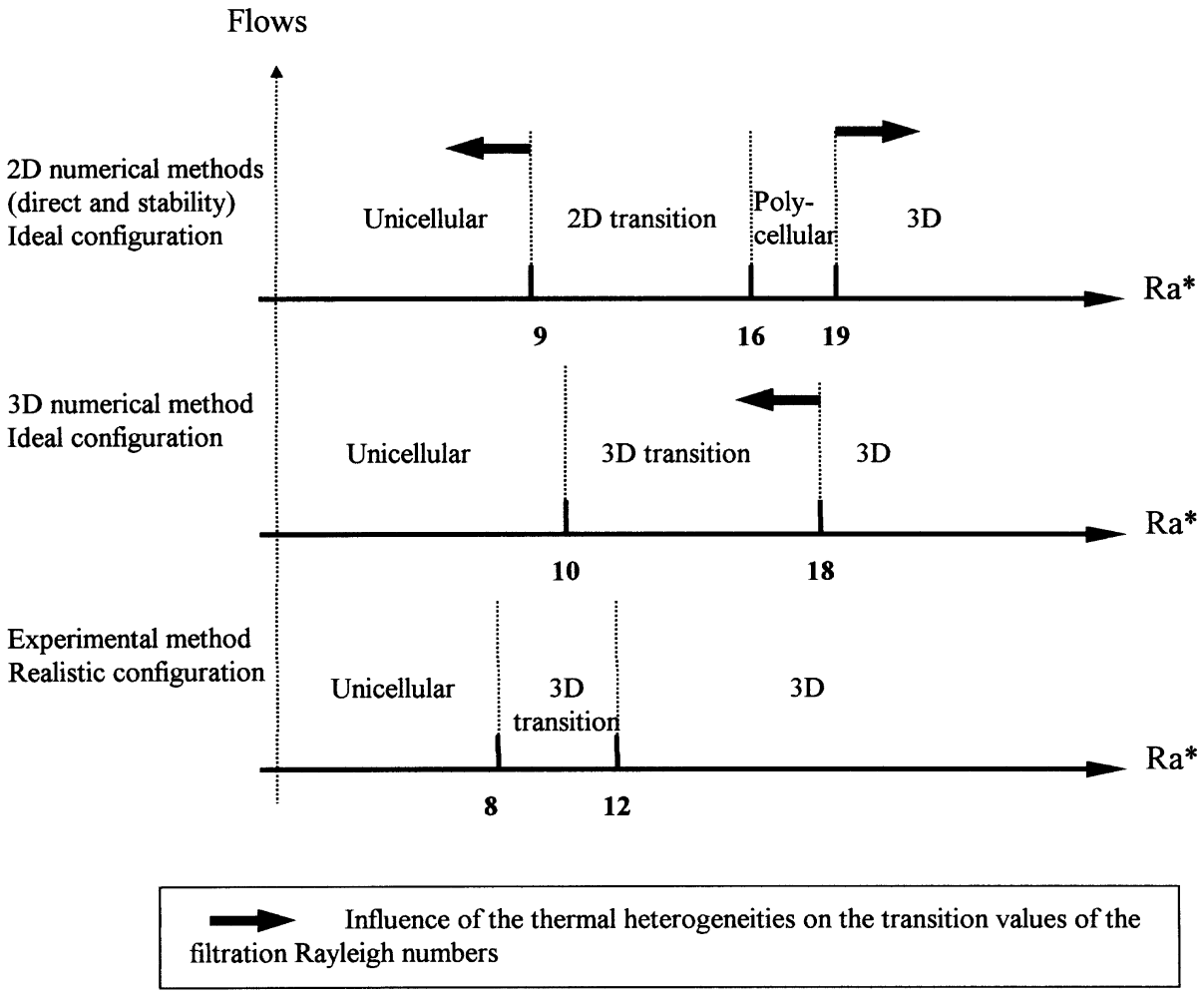

Fig. 11. Flow patterns appearing in the ideal finite layer as a function of Ra^* and the study methods ($\phi = 15^\circ$ and $\Lambda_p = 0.7$).

sition from unicellular to 3D flow appears for a lower Ra^* value due to the thermal losses. The lower Ra^* value for experimental 2D/3D transition than that for the numerical one can be so explained.

Both stability study and infinite configuration study indicate the occurrence of transversal rolls before longitudinal ones. However, the Ra^* values for the appearance of each type of rolls are close [13]. The experimental difficulties to distinguish the 3D flow establishment were also expected. 3D direct computations do not allow us to determine distinctly which rolls (transversal or horizontal) appear first.

7.2. 3D patterns

The elementary components of the 3D flows obtained by each method of resolution are described in Table 2. The most significant remark is that for all methods seven rolls constitute the transversal part of the 3D flow. Experimentally, five horizontal rolls occur at first in the porous layer, however at steady state, an additional roll has appeared in the medium [22]. Numerical and experimental 3D flows obtained for the realistic configuration are composed of an even number of longitudinal rolls. On both sloped sides of the layer, the fluid moves from the top to the bottom of the medium.

7.3. Amplitude of convection

Due to the linearization assumption, the stability analysis does not allow us to be conclusive in terms of perturbation range. The 3D resolutions lead to higher convective phenomena than 2D ones. For filtration Rayleigh number corresponding to 3D flow, the 2D numerical resolution does not allow us to determine the most stable flow which develops in the configuration. The 2D flow

Table 2
Elementary components of the 3D flows

Resolution methods	Number of transversal rolls (horizontal axis)	Number of longitudinal rolls (sloped axis)
2D direct computations: ideal and realistic configurations	7	—
Stability analysis: ideal and realistic configurations	7	5
3D direct computations: ideal configuration	7	7
3D direct computations: realistic configuration	7	8
3D experimental method	7	6

Flows are determined in each direction, each method and for the ideal and the realistic finite layers.

obtained has no real significance. The experimental flows have a higher amplitude than 3D numerical ones. However this phenomenon is located on the borders of the porous layer. In the central part of the medium, the influence of the flows is lower for experimental results than numerical ones.

3D numerical results of the realistic layer and experimental ones have common characteristics. Both show a more significant phenomenon of convection on the borders of the layer than in central part (Figs 5b and 8d). This particularity can be attributed to the imperfect adiabaticity of the sides. Moreover, the 3D numerical results suggest that the existence of a supplementary roll in 3D experimental flow can be attributed to the lateral thermal losses.

The uniformity of the upper and lower isothermal conditions is not as perfect for the experiment as for numerical resolutions. These imperfect thermal conditions, in addition to the lateral thermal losses, are an eventual explanation for the low amplitude of the rolls in the central part of the layer middle plane.

8. Conclusions

The work presented here concerns the phenomenon of natural convection appearing in a saturated porous layer bounded by impervious domains subjected to a vertical thermal gradient. Three configurations are considered: an infinite layer, a finite layer with adiabatic lateral conditions and a finite layer with lateral thermal losses. The experimental and numerical results lead to the following conclusive remarks.

The phenomenon is restricted by the thermal boundary conditions. The upper and lower thermal limits, characterized by the filtration Rayleigh number, influence directly the convection patterns and ranges. The lateral thermal conditions influence the flows indirectly. The thermal losses destabilize the 2D basic unicellular flow and affect the convective perturbation in the third direction (they modify the number of transversal rolls which appear).

The numerical and experimental resolutions were necessary and complementary for a better knowledge of the phenomenon. They allow us to determine the most influential parameters of the convection. In our study, the comparison of the two methods put into evidence the significant influence of the thermal boundary conditions on the phenomenon.

The reference configurations were defined to represent the geological structures. This study has demonstrated that the finite dimensions of numerical and experimental configurations do not allow us to translate directly the results to natural sites. However the pertinence of the models has been proved. The numerical studies can be adequately used to simulate the natural convection phenomenon in real configurations, taking into account the complexity of the natural environment with special care to the thermal boundary conditions.

Acknowledgement

The authors wish to gratefully thank Mr Jean-Paul Grenet, from C.N.R.S., for his essential participation in the realization of the experimental apparatus.

References

[1] D.A. Nield, A. Bejan, Convection in Porous Media, 1st ed., Springer-Verlag, New York, 1991, p. 408.
[2] Y. Katto, T. Masuoka, Criterion for the onset of convective flow in a fluid in a porous medium, Int. J. Heat Mass Transfer 10 (1966) 297–309.
[3] D.A. Nield, Onset of thermohaline convection in a porous medium, Water Resources Res. 11 (1968) 553–560.
[4] S. Bories, C. Thirriot, Echanges thermiques et tourbillons dans une couche poreuse horizontale, La Houille Blanche 3 (1969) 237–245.

[5] J.P. Caltagirone, M. Cloupeau, M. Combarnous, Convection naturelle fluctuante dans une couche poreuse horizontale. C. R. Acad. Sci. 273 (1971) 833–836.
[6] J.P. Caltagirone, G. Meyer, A. Mojtabi, Structurations thermoconvectives tridimensionnelles dans une couche poreuse horizontale. J. de Mécanique 20 (2) (1981) 219–232.
[7] M. Combarnous, Convection naturelle et convection mixte en milieu poreux, Ph.D. thesis, Faculté des Sciences de l'Université de Paris, Paris, France, 1970.
[8] T. Kaneko, M.F. Mohtadi, K. Aziz, An experimental study of natural convection in inclined porous layer, Int. J. Heat Mass Transfer 17 (1973) 485–496.
[9] J.P. Caltagirone, S. Bories, Solutions and stability criteria of natural convective flow in an inclined porous layer, J. Fluid Mech. 155 (1985) 267–287.
[10] H. Inaba, M. Sugawara, J. Blumenberg, Natural convection heat transfer in an inclined porous layer, Int. J. Heat Mass Transfer 31 (7) (1988) 1365–1374.
[11] A. Ormond, P. Genthon, 3D thermoconvection in an anisotropic inclined sedimentary layer, Geophys. J. Int. 112 (1993) 257–263.
[12] N. Riahi, Nonlinear convection in a porous layer with finite conducting boundaries. J. Fluid Mech. 129 (1983) 153–171.
[13] N. Joly, Convection naturelle dans les structures géologiques poreuses: étude de stabilité d'un cas de référence et effet des failles, Ph.D. thesis, Université Bordeaux I, Bordeaux, France, 1994.
[14] S.J. Linz, A.W. Woods, Natural convection Taylor dispersion and diagenesis in a tilted porous layer, Phys. Rev. 46 (8) (1992) 4469–4878.
[15] N. Joly, D. Bernard, P. Ménégazzi, ST2D3D: A finite element program to compute stability criteria for natural convection in complex porous structures, Num. Heat Transfer 29 (B) (1996) 91–112.
[16] P. Gouze, A. Coudrain-Ribstein, D. Bernard, Computation of porosity redistribution resulting from thermal convection in slanted porous layers. J. Geophysical Res. 99 (B1) (1994) 697–706.
[17] M. Combarnous, S. Bories, Hydrothermal convection in saturated porous media. Adv. in Hydrosci. 10 (1975) 231–307.
[18] D. Bernard, Convection naturelle dans les structures géologiques poreuses: deux exemples numériques, Bull. Minéral. 111 (1988) 601–611.
[19] D.K. Gartling, C.E. Hickox, Numerical study of applicability of the Boussinesq approximation for a fluid saturated porous medium, Int. Journal for Num. Meth. in Fluid 5 (1985) 995–1013.
[20] D. Bernard, Convection naturelle dans une couche poreuse inclinée, in: Ouazard, Brebbia (Eds.), Proceedings of International Conference on Computer Methods and Water Resources, 14–18 March, Rabat, Morocco, Vol. 5: Computational Transport Phenomena, Comp. Mech. Pub., Southampton, 1988, pp. 59–70.
[21] M. Bernadou, P.L. George, A. Hassim, P. Joly, A. Perronnet, E. Saltel, D. Steer, G. Vanderborck, M. Vidrascu, MODULEF une bibliothèque modulaire d'éléments finis, INRIA, France, 1985, p. 503.
[22] S. Chevalier, Études numériques et expérimentale de la convection naturelle dans une couche poreuse inclinée: effets des conditions aux limites thermiques sur la structure des écoulements, Ph.D. thesis, Université Bordeaux I, Bordeaux, France, 1995.
[23] N. Joly, S. Chevalier, D. Bernard, Nature et stabilité des régimes d'écoulement de convection naturelle dans une couche poreuse inclinée limitée par des épontes imparfaitement conductrices de la chaleur, Proceedings of the Annual Congress of the French Society of Thermicians, CNAM, Paris, France, 1994, pp. 244–249.